OPEN ACCESS

Applied Physics Express 18, 116501 (2025) LETTER

https://doi.org/10.35848/1882-0786/ae1e59

Fabrication of β-Ga_2O_3/air-gap structures on (010) β-Ga_2O_3 by wet etching in tetramethylammonium hydroxide (TMAH)

Takayoshi Oshima*

Research Center for Electronic and Optical Materials, National Institute for Materials Science, Tsukuba, Ibaraki 305-0044, Japan

*E-mail: OSHIMA.Takayoshi@nims.go.jp

Received October 23, 2025; revised November 5, 2025; accepted November 10, 2025; published online November 25, 2025

We demonstrated the fabrication of β-Ga_2O_3/air-gap structures on (010) β-Ga_2O_3 substrates through sequential dry etching and crystallographic wet etching. Wet etching in a 25 wt% tetramethylammonium hydroxide solution at 90 °C yielded a lateral-to-vertical etch-rate ratio of approximately 11 when the lateral direction was aligned with [001]. This pronounced lateral etching enabled the undercutting of dry-etched β-Ga_2O_3 mesas to form cantilevers and air bridges extending along [201], which is perpendicular to [001]. This etch-only process using standard device-fabrication equipment offers a straightforward route for fabricating β-Ga_2O_3/air-gap structures that are promising for microelectromechanical systems. © 2025 The Author(s). Published on behalf of The Japan Society of Applied Physics by IOP Publishing Ltd

β-Ga_2O_3 is an emerging compound semiconductor that has attracted considerable attention owing to its wide range of applications. With a wide bandgap of 4.4–4.9 eV and a large critical electric field of approximately 8 MV cm^{-1},[1–4] β-Ga_2O_3 holds great promise for power electronic and deep-ultraviolet optical applications.[5] Moreover, its electrical conductivity is sensitive to both reducing and oxidizing gases, paving the way for gas-sensing applications.[6,7] It also exhibits high tolerance to elevated temperatures and radiation, making the devices suitable for operation in harsh environments.[8–12] Furthermore, it possesses mechanical properties comparable to those of Si, suggesting strong potential for future applications in microelectromechanical systems (MEMS).[13] In particular, β-Ga_2O_3 MEMS devices are expected to exhibit unique functionalities beyond those achievable with Si, such as harsh-environment actuators and resonant sensors, as well as resonance-based components (e.g. filters, mixers, and frequency references for on-chip oscillators) that can complement β-Ga_2O_3 power and RF devices.[13] To date, several β-Ga_2O_3-based MEMS devices, including resonators,[14–16] and resonant deep-ultraviolet detectors,[17,18] pressure sensors,[19] and transistors[20] have been demonstrated, underscoring its potential for MEMS technologies.

However, previously demonstrated β-Ga_2O_3-based MEMS have faced a critical challenge in the fabrication of β-Ga_2O_3/air-gap structures, such as diaphragms[14,16,17] and air bridges.[15,16,18–20] These structures were fabricated by manually transferring β-Ga_2O_3 flakes—either low-pressure chemical vapor deposition (LPCVD)-grown[14,17] or exfoliated from bulk single crystals[15,16,18–20]—onto prepatterned foreign substrates, resulting in poor reproducibility. For practical applications, β-Ga_2O_3/air-gap structures should be fabricated through highly reproducible and controllable processes. Considering the current Si MEMS fabrication technology, crystallographic etching should be a promising approach for this purpose.[21]

Crystallographic etching of β-Ga_2O_3 has recently attracted significant research interest. Both gas-phase etching using HCl gas,[22–29] forming gas,[30,31] Ga flux,[32–35] and triethylgallium gas[31,36,37] and wet chemical etching with H_3PO_4[31,38–40] and Pt metal and a mixture of HF and $K_2S_2O_8$ (MacEtch)[41,42] have been demonstrated on β-Ga_2O_3 substrates with various substrate orientations, including (100),[28,38] (010),[24,31,32,35–37,40–42] (001),[22,23,27,29,31–33,36,37,39] $(\bar{2}\ 01)$,[31,34] $(\bar{1}\ 02)$,[25,30] and (011),[26] primarily for fabricating fins and trenches with plasma-damage-free sidewalls to improve electronic device performances.[33,41,42] Furthermore, even β-Ga_2O_3/air-gap structures—such as cantilevers and air bridges, which are fundamental MEMS components—have been achieved using HCl gas etching on (100) and (001) β-Ga_2O_3 substrates by exploiting the strong lateral etching capability along the ⟨010⟩ directions relative to the vertical ones.[28,29] These demonstrations highlight the potential of crystallographic etching of β-Ga_2O_3 even for MEMS applications.

In this study, we explore the feasibility of fabricating β-Ga_2O_3/air-gap structures through crystallographic wet etching. Crystallographic gas etching demands specialized systems such as halide vapor-phase epitaxy,[22–29] metal-organic chemical vapor deposition,[31,36,37] molecular beam epitaxy,[32,33] LPCVD,[34,35] a gas-flow annealing furnace.[30] In contrast, wet etching can be performed using a simple chemical bath, thereby substantially reducing the etching cost. However, air-gap formation by wet etching has not yet been realized. Therefore, this study aims to verify whether crystallographic wet etching can achieve sufficient anisotropy for air-gap formation in β-Ga_2O_3. For the experiments, (010)-oriented substrates were employed because this surface orientation exhibits high etch resistance to wet etchants,[40] with the expectation of faster lateral than vertical etching, suitable for air-gap formation.[28] In addition, we selected tetramethylammonium hydroxide (TMAH) as the wet etchant. Although TMAH has not previously been applied to the crystallographic etching of β-Ga_2O_3, it has demonstrated effectiveness in forming step-and-terrace surfaces[43] and in removing dry-etch-induced roughness and damage,[44–47] indicating its suitability as a wet etchant.

We conducted systematic experiments similar to the air-gap formation demonstrated in our previous HCl gas etching study.[29] Two Sn-doped, conductive (010) β-Ga_2O_3 substrates with a nominal carrier density of 2.8×10^{18} cm^{-3} (Samples A and B) were used. Sample A was employed to investigate the in-plane anisotropy of side etching, and Sample B to demonstrate the fabrication of β-Ga_2O_3/air-gap structures. The process sequences for the two samples are shown in Fig. 1.

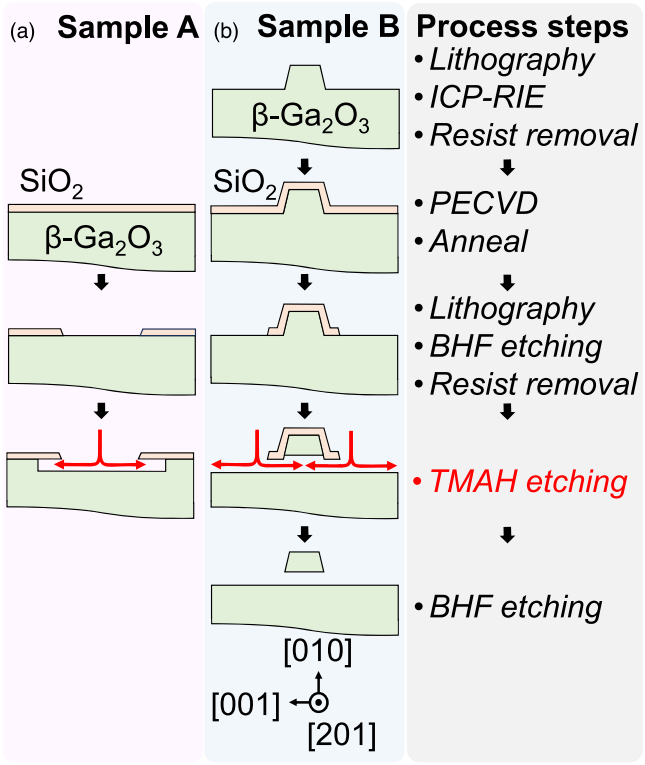

Fig. 1. Schematic illustrations of the process sequences for (a) investigating in-plane side-etching behavior (Sample A) and (b) fabricating β-Ga_2O_3/air-gap structures (Sample B).

For Sample A [Fig. 1(a)], a 0.14 μm thick SiO_2 masking layer was deposited by plasma-enhanced chemical vapor deposition (Samco, PD-220NL). Subsequently, the sample was annealed at 900 °C in an N_2 atmosphere under atmospheric pressure for 1 h to densify the layer and improve etch resistance.[48] Wagon-wheel-shaped etching windows—comprising 72 linear openings arranged at 5° intervals from the [102] direction—were then prepared by laser lithography (Heidelberg Instruments, DWL66$^+$), followed by buffered hydrofluoric acid (BHF) etching. The photoresist was removed by organic cleaning in N-methyl-2-pyrrolidone and isopropyl alcohol, followed by oxygen plasma ashing. The resulting linear windows were 50 μm in length and 1.5 μm in width. Finally, wet etching was performed in a 25 wt% TMAH solution at 90 °C for 1.5 h using a laboratory made polytetrafluoroethylene container, which was heated on a hot-plate stirrer.

It should be noted that 90 °C is the practical temperature limit of the 25 wt% TMAH solution,[44–46] as its boiling point is 103 °C. Since the wet etch rate was assumed to vary exponentially according to the Arrhenius relation,[38–40] the etching temperature was precisely monitored and controlled using a perfluoroalkoxy-coated thermocouple immersed in the solution, which was continuously stirred to ensure temperature uniformity. In addition, to maintain a constant TMAH concentration, the etching container was equipped with a sealable lid, allowing vapor to condense and reflux back into the solution.

For Sample B [Fig. 1(b)], mesa structures were fabricated by defining the mesa regions via laser lithography, followed by inductively coupled plasma reactive ion etching (ICP-RIE, Samco RIE-101iPH) using BCl_3 and Ar. The photoresist was then removed using the same procedure described above, and the redeposited materials were subsequently removed by HNO_3 etching at room temperature. The resulting mesas, approximately 30.6 μm in length, 2.5 μm in width, and 1.03 μm in height were aligned along the [201] direction; the reason for selecting this orientation will be discussed later. A 0.12 μm thick SiO_2 masking layer was subsequently deposited and annealed under the same conditions as Sample A. Etching windows were then formed by sequential laser lithography, BHF etching, and photoresist removal, leaving the mesa tops and sidewalls covered with the mask. Finally, wet etching in a 25 wt% TMAH solution at 90 °C for 6 h produced air gaps, after which the mask was removed by BHF etching.

In this process, the geometry of the β-Ga_2O_3/air-gap structures reflected that of the mesa patterns. The mesa height was defined by the dry-etch depth, which is controlled within 5% accuracy (specification of RIE-101iPH). The lateral width was defined by the photoresist mask patterned by laser lithography, with a critical dimension uniformity of 0.06 μm (specification of DWL66$^+$), corresponding to 3% accuracy for a 2.5 μm wide mesa. Because the resonant frequency of cantilevers and air bridges is proportional to the structure height according to the well-known Euler–Bernoulli beam model, the process equipment used in this study may cause variations in the resonant frequency of up to approximately 5%. Such a deviation is acceptable for research and prototyping purposes; however, for practical implementation, higher process precision within 1% would be required, necessitating a dry-etching system with improved depth control accuracy.

The resulting etched structures were characterized using differential interference contrast (DIC) microscopy, scanning electron microscopy (SEM), and atomic force microscopy (AFM). Focused ion beam milling (FIB) was also employed for the cross-sectional SEM observation.

We first investigated the in-plane side-etching behavior. Figure 2 summarizes the results obtained from the etched trenches formed beneath the wagon-wheel windows on Sample A.

Figure 2(a) shows a DIC image of the upper half of the wagon-wheel-patterned trenches. Owing to the twofold rotational symmetry around the [010] axis on the (010) plane,[49] the lower half is omitted. The mask was not removed; therefore, the side-etched regions appear in a different color from the substrate surface and the linear windows. The side etching was clearly anisotropic. Trenches oriented near the [201] direction exhibited pronounced side etching, as shown in the enlarged image [Fig. 2(b)], indicating that the lateral etching was most enhanced in directions close to ⟨001⟩. Figure 2(c) presents a polar plot of the side-etch rate, constructed from the side-etch lengths measured using DIC microscopy and SEM. The plot exhibits twofold rotational symmetry, reflecting the crystallographic symmetry on the (010) plane.[49] The maximum side-etch rates were 0.76 μm h^{-1} in directions approximately along ⟨001⟩. In contrast, the rates along the ⟨201⟩ direction, which is perpendicular to ⟨001⟩, were as low as 0.05 μm h^{-1}. Such a large difference in etch rates between orthogonal in-plane directions is advantageous for forming cantilevers and air bridges, as the supporting regions remain largely intact

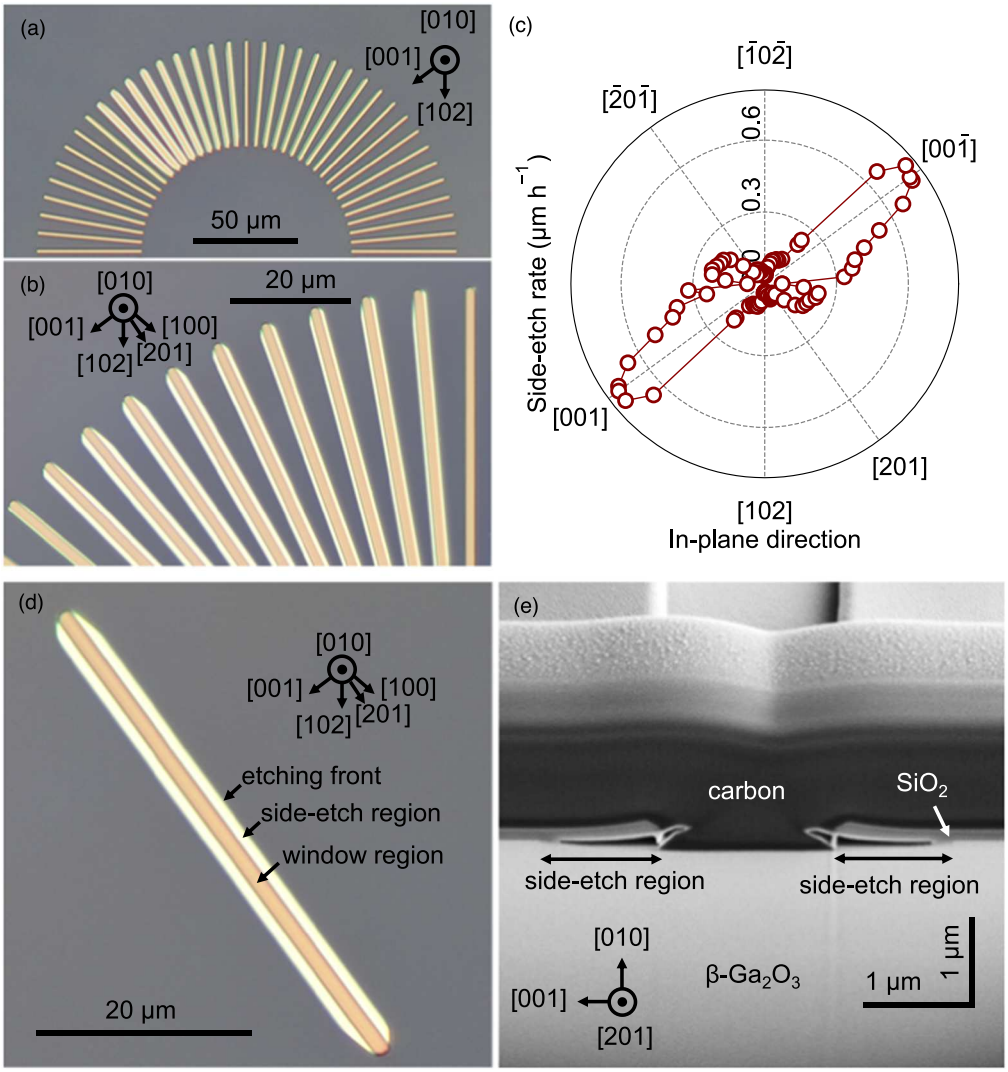

Fig. 2. Summary of the in-plane side-etching characteristics on a (010) β-Ga_2O_3 substrate (Sample A). (a) DIC image showing side-etched structures formed beneath a wagon-wheel window pattern. (b) Enlarged view of the region with the larger side etching in (a). (c) Polar plot of side-etch rates perpendicular to the wagon-wheel windows shown in (a). (d) DIC image of the etched structure formed beneath a linear window aligned with the [201] direction. (e) 54°-tilted SEM image of the cross section of the etched structure shown in (d).

during side etching. Therefore, cantilevers and air bridges were designed along the [201] direction.

Figure 2(d) shows a DIC image of an etched trench formed beneath a linear window aligned along the [201] direction. The shapes of the side-etched regions on both sides of the linear trench were almost identical, except at both ends, where the etching fronts were parallel to the [102] and [100] directions, suggesting the development of ($\bar{2}$01) and (001) facets, respectively. Figure 2(e) presents a 54°-tilted cross-sectional SEM image of the [201]-oriented etched trench. The FIB-exposed plane corresponds to (100), which is perpendicular to [201]. The etched depth within the window region was as small as 0.10 μm, whereas the side-etched length reached 1.13 μm. Such a high lateral-to-vertical etch-rate ratio of approximately 11 enables the formation of air gaps. Notably, the bottom surface in the side-etched regions was not parallel to the (010) plane but slightly curved upward toward etch fronts.

We then carried out air-gap formation to achieve β-Ga_2O_3/air-gap structures. Figure 3 summarizes the results of the fabricated cantilever and air bridge on Sample B.

Figures 3(a) and 3(b) present oblique-view SEM images of the cantilever and air bridge extending along the [201] direction, respectively. Dark shadows were observed beneath both structures, confirming the formation of air gaps resulting from the pronounced lateral etching along the ⟨001⟩ directions, which are perpendicular to [201]. In contrast, no shadows appeared on the etched sidewalls parallel to the [001] direction, consistent with the weak lateral etching along the ⟨201⟩ directions. The grooved, rough sidewall morphology of both structures originated from ICP-RIE, which could be smoothed by optimizing the dry-etching conditions. Figure 3(c) shows a 54°-tilted cross-sectional image taken at the midpoint of the air bridge, where the exposed plane corresponds to (100). A distinct air gap was clearly visible. The air-gap spacing was smaller at the center (0.26 μm) than at the ends (0.52 μm), consistent with the lateral etching characteristics along the ⟨001⟩ directions described previously in Fig. 2(e). The reverse side of the air bridge also exhibited inclinations in opposite directions to the bottom surface, owing to the mirror symmetry with respect to the (010) plane.[49] The bridge thickness was 0.63–0.85 μm, smaller than the initial mesa height of 1.03 μm, because wet etching slowly proceeded from the reverse side as well. Although the gap spacing was small for MEMS

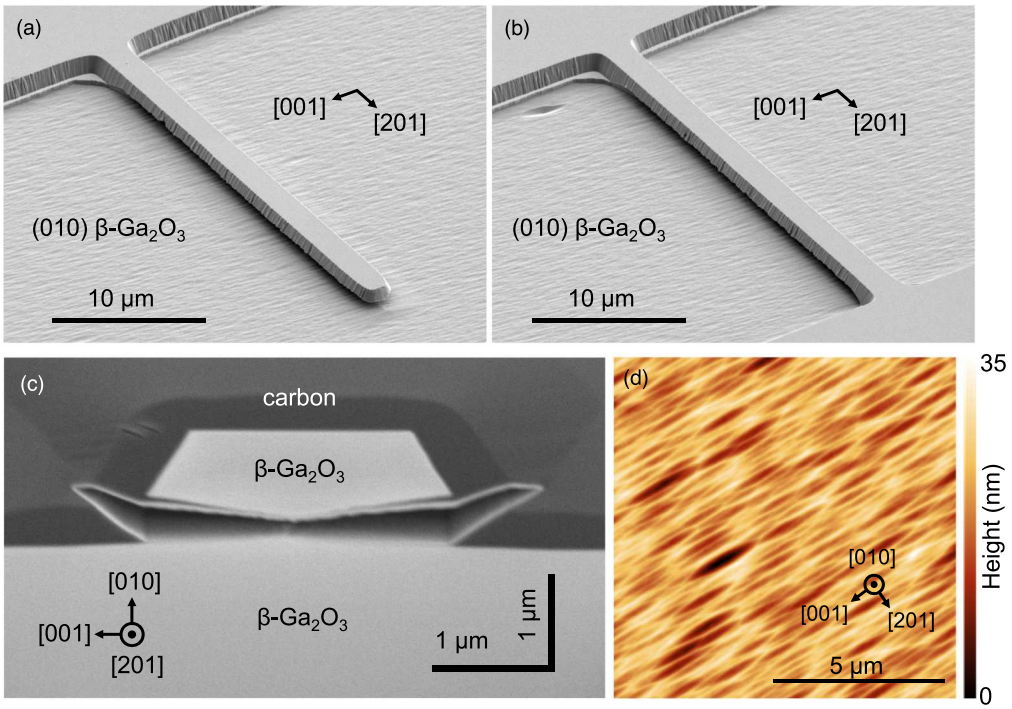

Fig. 3. 54°-tilted SEM images of the fabricated (a) cantilever and (b) air bridge on a (010) β-Ga_2O_3 substrate (Sample B). (c) 54°-tilted cross-sectional SEM image corresponding to the air bridge shown in (b). (d) AFM image of the TMAH-etched bottom surface.

applications, it could be increased by performing Cl-based ICP-RIE of both SiO_2 and β-Ga_2O_3, instead of BHF etching of SiO_2 alone, prior to TMAH etching.

Aside from the β-Ga_2O_3/air-gap structures, the TMAH-etched (010) bottom surface exhibited a smooth yet nonflat morphology [Figs. 3(a), 3(b), and 3(d)]. Other crystal facets extending along the [001] direction preferentially developed in place of the (010) plane. Therefore, the high etch resistance observed on the (010) surface was actually attributed not to the (010) plane itself, but to these crystallographic planes. The root-mean-square roughness of the surface was 4.4 nm, as revealed by the AFM image shown in Fig. 3(d). Considering the mirror symmetry, a similar surface roughness is expected on the reverse side of the cantilever and air bridge. Such sub-10 nm roughness is sufficient to achieve quality factors on the order of 10^4–10^5 in MEMS resonators.[50)]

In conclusion, we demonstrated the fabrication of β-Ga_2O_3/air-gap structures on a (010)-oriented substrate. The key processing step was crystallographic wet etching in heated TMAH, where the lateral etch rates along the ⟨001⟩ directions were sufficiently higher than the vertical etch rate on the (010) plane, enabling the formation of air gaps for fabricating cantilevers and air bridges. These results highlight the strong potential of crystallographic wet etching of β-Ga_2O_3 and are expected to stimulate future research on β-Ga_2O_3-based MEMS.

Acknowledgments This study was supported by the Materials Forming Unit and the Nanofabrication Microscopy Unit at the NIMS within the framework of the Advanced Research Infrastructure for Materials and Nanotechnology (ARIM), supported by the Ministry of Education, Culture, Sports, Science and Technology (MEXT), Japan (No. JPMXP1225NM5079). This work was financially supported by a Grant-in-Aid for Scientific Research (B) from the Japan Society for the Promotion of Science (JSPS), MEXT, Japan (No. JP24K01368).

ORCID iDs Takayoshi Oshima https://orcid.org/0000-0001-8550-9735

1) T. Onuma, S. Saito, K. Sasaki, T. Masui, T. Yamaguchi, T. Honda, and M. Higashiwaki, Jpn. J. Appl. Phys. **54**, 112601 (2015).
2) M. Higashiwaki, K. Sasaki, A. Kuramata, T. Masui, and S. Yamakoshi, Appl. Phys. Lett. **100**, 013504 (2012).
3) T. Oshima, M. Hashikawa, S. Tomizawa, K. Miki, T. Oishi, K. Sasaki, and A. Kuramata, Appl. Phys. Express **11**, 112202 (2018).
4) Z. Xia et al., Appl. Phys. Lett. **115**, 252104 (2019).
5) S. J. Pearton, F. Ren, A. Y. Polyakov, A. Haque, M. Labed, and Y. S. Rim, Appl. Phys. Rev. **12**, 031336 (2025).
6) M. Bartic, Y. Toyoda, C.-I. Baban, and M. Ogita, Jpn. J. Appl. Phys. **45**, 5186 (2006).
7) S. Jang, S. Jung, J. Kim, F. Ren, S. J. Pearton, and K. H. Baik, ECS J. Solid State Sci. Technol. **7**, Q3180 (2018).
8) C. Hou, K. R. York, R. A. Makin, S. M. Durbin, R. M. Gazoni, R. J. Reeves, and M. W. Allen, Appl. Phys. Lett. **117**, 203502 (2020).
9) A. E. Islam et al., Appl. Phys. Lett. **121**, 243501 (2022).
10) W. A. Callahan, K. Egbo, C.-W. Lee, D. Ginley, R. O'Hayre, and A. Zakutayev, Appl. Phys. Lett. **124** (2024)153504.
11) M. H. Wong, A. Takeyama, T. Makino, T. Ohshima, K. Sasaki, A. Kuramata, S. Yamakoshi, and M. Higashiwaki, Appl. Phys. Lett. **112**, 023503 (2018).
12) S. A. Khan, S. Saha, U. Singisetti, and A. F. M. A. U. Bhuiyan, J. Appl. Phys. **136**, 225701 (2024).
13) X.-Q. Zheng, H. Zhao, and P. X. L. Feng, Appl. Phys. Lett. **120**, 040502 (2022).
14) X.-Q. Zheng, J. Lee, S. Rafique, L. Han, C. A. Zorman, H. Zhao, and P. X. L. Feng, ACS Appl. Mater. Interfaces **9**, 43090 (2017).
15) M. Peres et al., ECS J. Solid State Sci. Technol. **8**, Q3235 (2019).
16) X.-Q. Zheng, H. Zhao, Z. Jia, X. Tao, and P. X. L. Feng, Appl. Phys. Lett. **119**, 013505 (2021).
17) X.-Q. Zheng, J. Lee, S. Rafique, M. R. Karim, L. Han, H. Zhao, C. A. Zorman, and P. X. L. Feng, IEEE Electron Device Lett. **39**, 1230 (2018).
18) X.-Q. Zheng, Y. Xie, J. Lee, Z. Jia, X. Tao, and P. X. L. Feng, APL Mater. **7**, 022523 (2019).
19) W. Sui, S. M. Enamul Hoque Yousuf, Y. Liu, S. J. Pearton, and P. X. L. Feng, Adv. Mater. Technol. **9**, 2301356 (2024).
20) X.-Q. Zheng, T. Kaisar, and P. X.-L. Feng, Appl. Phys. Lett. **117**, 243504 (2020).
21) W. Lang, Mater. Sci. Eng. R **17**, 1 (1996).
22) T. Oshima and Y. Oshima, Appl. Phys. Lett. **122**, 162102 (2023).
23) Y. Oshima and T. Oshima, Jpn. J. Appl. Phys. **62**, 080901 (2023).
24) T. Oshima and Y. Oshima, Appl. Phys. Express **16**, 066501 (2023).
25) T. Oshima and Y. Oshima, Appl. Phys. Lett. **124**, 042110 (2024).

26) T. Oshima and Y. Oshima, Jpn. J. Appl. Phys. **64**, 018003 (2025).
27) Y. Oshima and T. Oshima, Sci. Technol. Adv. Mater. **26**, 2546285 (2025).
28) T. Oshima and Y. Oshima, AIP Adv. **15**, 055207 (2025).
29) T. Oshima and Y. Oshima, Sci. Technol. Adv. Mater. Methods **5**, 2554046 (2025).
30) T. Oshima, R. Togashi, and Y. Oshima, Sci. Technol. Adv. Mater. **25**, 2378683 (2024).
31) L. Meng, V. G. Thirupakuzi Vangipuram, D. S. Yu, C. Hu, and H. Zhao, J. Vac. Sci. Technol. B **43**, 052201 (2025).
32) N. K. Kalarickal et al., Appl. Phys. Lett. **119**, 123503 (2021).
33) S. Dhara, N. K. Kalarickal, A. Dheenan, S. I. Rahman, C. Joishi, and S. Rajan, Appl. Phys. Lett. **123**, 023503 (2023).
34) D. Kumar and A. Verma, J. Vac. Sci. Technol. A **43**, 053405 (2025).
35) S. A. Khan, A. Ibreljic, and A. F. M. A. U. Bhuiyan, Appl. Phys. Lett. **127**, 102105 (2025).
36) A. Katta, F. Alema, W. Brand, A. Gilankar, A. Osinsky, and N. K. Kalarickal, J. Appl. Phys. **135**, 075705 (2024).
37) N. Das, F. Alema, W. Brand, A. Katta, A. Gilankar, A. Osinsky, and N. K. Kalarickal, J. Appl. Phys. **138**, 065703 (2025).
38) T. Oshima, T. Okuno, N. Arai, Y. Kobayashi, and S. Fujita, Jpn. J. Appl. Phys. **48**, 040208 (2009).
39) S. Rebollo, T. Itoh, S. Krishnamoorthy, and J. S. Speck, Appl. Phys. Lett. **125**, 012102 (2024).
40) Y. Zhang, A. Mauze, and J. S. Speck, Appl. Phys. Lett. **115**, 013501 (2019).
41) H. Huang, M. Kim, X. Zhan, K. Chabak, J. D. Kim, A. Kvit, D. Liu, Z. Ma, J.-M. Zuo, and X. Li, ACS Nano **13**, 8784 (2019).
42) H.-C. Huang et al., Appl. Phys. Lett. **121**, 052102 (2022).
43) T. Oshima, Jpn. J. Appl. Phys. **64**, 088001 (2025).
44) H.-K. Lee, H.-J. Yun, K.-H. Shim, H.-G. Park, T.-H. Jang, S.-N. Lee, and C.-J. Choi, Appl. Surf. Sci. **506**, 144673 (2020).
45) X. Lu, T. Xu, Y. Deng, C. Liao, H. Luo, Y. Pei, Z. Chen, Y. Lv, and G. Wang, Appl. Surf. Sci. **597**, 153587 (2022).
46) F. Zhang, X. F. Zheng, Y. H. Li, Z. J. Yuan, S. Z. Yue, X. C. Wang, Y. L. He, X. L. Lu, X. H. Ma, and Y. Hao, Appl. Surf. Sci. **684**, 161569 (2025).
47) A. R. Gutierrez et al., J. Vac. Sci. Technol. A **43**, 033210 (2025).
48) F. S. Becker, D. Pawlik, H. Anzinger, and A. Spitzer, J. Vac. Sci. Technol. B **5**, 1555 (1987).
49) J. Åhman, G. Svensson, and J. Albertsson, Acta Crystallogr., Sect. C **52**, 1336 (1996).
50) Z. Zhang, G. Chen, K. Gu, S. Koizumi, and M. Liao, Funct. Diam. **3**, 2221280 (2023).